### Title

Nanostructure Transformation as a Signature of Oxygen Redox in Li-Rich 3d and 4d Cathodes




### Journal

Journal of the American Chemical Society, 143(15)

### ISSN

0002-7863



### Authors

Grenier, Antonin
Kamm, Gabrielle E
Li, Yixuan
et al.



### Publication Date

2021-04-21

### DOI

10.1021/jacs.1c00497

Peer reviewed

# Nanostructure Transformation as a Signature of Oxygen Redox in Li-Rich 3d and 4d Cathodes

Antonin Grenier, Gabrielle E. Kamm, Yixuan Li, Hyeseung Chung, Ying Shirley Meng, and Karena W. Chapman*

**ABSTRACT:** Lithium-rich nickel manganese cobalt oxide (LRNMC) is being explored as an alternative to stoichiometric nickel manganese cobalt oxide (NMC) cathode materials due to its higher, initially accessible, energy-storage capacity. This higher capacity has been associated with reversible O oxidation; however, the mechanism through which the change in O chemistry is accommodated by the surrounding cathode structure remains incomplete, making it challenging to design strategies to mitigate poor electrode performance resulting from extended cycling. Focusing on LRNMC cathodes, we identify nanoscale domains of lower electron density within the cathode as a structural consequence of O oxidation using small-angle X-ray scattering (SAXS) and operando X-ray diffraction (XRD). A feature observed in the small angle scattering region suggests the formation of nanopores, which first appears during O oxidation, and is partially reversible. This feature is not present in traditional cathode materials, including stoichiometric NMC and lithium nickel cobalt aluminum oxide (NCA) but appears to be common to other Li-rich systems tested here, $Li_2RuO_3$ and $Li_{1.3}Nb_{0.3}Mn_{0.4}O_2$.

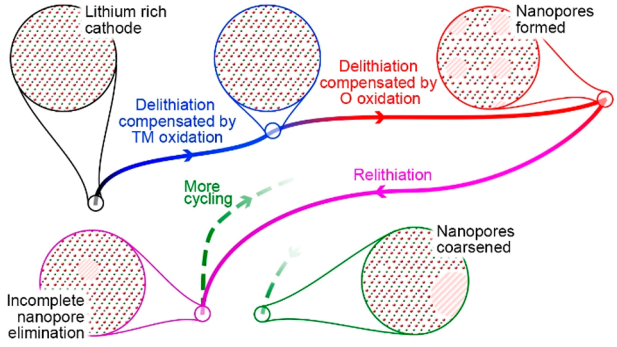


## INTRODUCTION

The recent discovery of reversible oxygen-based redox in lithium layered transition metal oxide (LTMO) positive electrodes offers a promising route to achieving higher-capacity Li-ion batteries.[1] Despite extensive efforts to understand this O redox phenomenon, the mechanism remains controversial.[2] First thought to only be present for the Li-rich LTMOs (with Li/TM ratio of >1), reversible oxygen redox has been reported in conventional stoichiometric LTMOs[3,4] (with Li/TM ratio of 1), Li-rich cation disordered rocksalts,[5] and even sodium transition metal oxides.[6] A clear, cohesive picture of the structural mechanism, and how the O redox is accommodated within the electrode structure, has yet to emerge.

Li-rich LTMOs such as $Li_xNi_{0.13}Mn_{0.54}Co_{0.13}O_2$ (LRNMC, $x > 1$) are among the most widely studied O-redox systems. LRNMC electrodes can achieve reversible capacities of over 300 mAh/g,[7] compared with capacities typically below 250 mAh/g for stoichiometric conventional counterparts like $Li_1Ni_yMn_zCo_{1-y-z}O_2$ (NMC) that are broadly used in electric vehicles. Understanding how the O-redox impacts the Li-rich electrode structure and how this may evolve with cycling is important to overcoming limitations related to poor energy inefficiency, voltage fade, and capacity fade that, at present, prevent their implementation in commercial batteries.

In LRNMC, O oxidation in the first charge is characterized by an additional charge plateau at 4.5 V that is not seen in stoichiometric NMC. Irreversible O loss only accounts for a fraction of the capacity obtained during the 4.5 V charge plateau,[8,9] with multiple spectroscopic techniques instead suggesting a mostly reversible bulk O oxidation.[1] Indeed, as no significant spectroscopic changes are observed at TMs' absorption edges, as would indicate changes in their oxidation state, oxidation during the 4.5 V plateau cannot be attributed to TM cations. Instead, resonant inelastic X-ray scattering (RIXS) measurements at the O's K-edge show that charge in the 4.5 V plateau gives rise to characteristic emissions that can be used as proxy for bulk oxidized O species.[8] The RIXS characteristic features disappear during subsequent discharge.[6]

Similar high-voltage plateaus involving O oxidation and reversible growth of RIXS features have been reported for a multitude of other Li-rich cathode materials such as layered $Li_2RuO_3$.[10] Unlike stoichiometric NMCs, these LR systems often show dramatic changes in the voltage profile following the first charge. Structural studies of LRNMC have demonstrated that O oxidation in the first charge is

accompanied by the migration of TMs to Li layers[11−13] and changes in the local Mn environment.[14] This migration leads to the elimination of the cation superstructure ordering in the TM layer which may account for the changes in the voltage profile; the original 4.5 V plateau and cation ordered superstructure can be restored with heating above 150 °C.[15]

Here we show, for the first time, that charge during O oxidation is accompanied by the formation of nanoscale domains of low density within the structure. Focusing on the LRNMC system and using a combination of small-angle X-ray scattering (SAXS) and operando X-ray diffraction (XRD), we show that an increased abundance of these low density nanoscale domains is characterized by the growth of scattering intensity at low angle, in the $Q$ range 0.1−1 Å$^{-1}$. On the basis of this observation, we propose that O oxidation leads to the nanostructuration of the LRNMC cathode involving the migration of the transition metal cations to stabilize the O oxidation reaction. Transition metal migration results in the formation of nanoscale domains of lower electron density or nanopores. The formation of nanopores is partially reversed during discharge, with progressive growth of the average low density domain size following multiple cycles. Comparison of the operando XRD data recorded for other compounds including $Li_2RuO_3$ and $Li_{1.3}Nb_{0.3}Mn_{0.4}O_2$ suggests that a similar mechanism is at play in all Li-rich electrode systems showing O-redox activity.

## EXPERIMENTAL SECTION

**Materials.** $Li_{1.144}Ni_{0.136}Mn_{0.544}Co_{0.136}O_2$ synthesis is described in detail elsewhere.[16] To summarize, aqueous solutions of Ni/Mn/Co nitrates and $Na_2CO_3$ were mixed in appropriate proportions at pH = 7.8 to yield the carbonate precursor $Ni_{1/6}Co_{1/6}Mn_{4/6}CO_3$. The carbonate precursor was mixed with $Li_2CO_3$ in a 0.7 molar ratio and heated to 500 °C for 5 h and 850 °C for 15 h in air. $Li_{1.3}Nb_{0.3}Mn_{0.4}O_2$ was prepared by heating a pelletized mixture of $Nb_2O_5$ (Alfa Aesar, >99.9985%), $Mn_2O_3$ (Strem, >99%), and 10% excess $Li_2CO_3$ (Sigma-Aldrich, >99%) for 24 h to 950 °C in argon. The precursors were first mixed by wet mechanical ball milling at 400 rpm for 2 h in a $ZrO_2$ jar using 5 mm diameter balls and isopropanol as solvent. $Li_2RuO_3$ was prepared by heating a pelletized, stoichiometric mixture of $RuO_2$ (Strem, >99.9%) and $Li_2CO_3$ (Acros, 99.999%) for 5 h at 950 °C in air. The precursors were first ball-milled for 15 min at 650 rpm in a $ZrO_2$ jar using 10 mm diameter balls. $Li_1Ni_{0.80}Co_{0.15}Al_{0.05}O_2$ (ref NAT-1050) and $Li_1Ni_{0.4}Mn_{0.4}Co_{0.2}O_2$ (ref NM-4100L) were obtained from Toda America. $Li_1Ni_{0.4}Mn_{0.4}Co_{0.2}O_2$ was heated to 500 °C for 3 h in air to remove surface species.[17] Characterization of the pristine materials is available Figures S1−S5.

Electrodes were prepared by grinding the active material with carbon black (Timcal Super C65) and PTFE powder (Sigma-Aldrich, 1 $\mu$m particle size) in a 7:1:2 weight ratio, using an agate mortar and pestle. For $Li_{1.3}Nb_{0.3}Mn_{0.4}O_2$, the material was first ball-milled (2 h at 300 rpm in a $ZrO_2$ jar using 3 mm balls) with the carbon black in a 4:1 weight ratio before adding 20 wt % PTFE powder. The electrode mixture was pressed into pellets using a hand press and assembled into cells using $LiPF_6$ dissolved in an ethylene carbonate−dimethyl carbonate mixture (1:1 ratio in volume) as electrolyte (Sigma-Aldrich), glass fiber (Whatman GF/B) and Celgard 3401 as separators, and Li foil (MTI Corp) as counter electrode.

Material storage, electrode preparation, and cell (dis)assembly were all carried out in an argon-filled glovebox (<0.5 ppm of $O_2$ and $H_2O$).

**Scanning Electron Microscopy.** Cross-sectional SEM results of pristine LRNMC were collected using a focused ion beam-SEM (Scios 2 DualBeam). About 800 nm of Pt was deposited on the top of the particle before cutting to minimize beam damage.

**Operando Synchrotron X-ray Diffraction and Pair Distribution Function Analysis during Electrochemical Cycling.** Three mm-diameter pressed-pellet electrodes (~6 mg) were cycled at 23.82 mA·g$^{-1}$ (~C/15) in RATIX[18]-type cells using a BioLogic BCS-800 cycler. Time-resolved X-ray scattering data suitable for diffraction (XRD, $Q_{max} \approx 6.2$ Å$^{-1}$) and pair distribution function (PDF, $Q_{max} \approx 25.5$ Å$^{-1}$) analysis were recorded sequentially on multiple RATIX cells using high-energy X-rays ($\lambda$ = 0.1668 Å) provided by beamline 28-ID-1 of the National Synchrotron Light Source II (NSLS-II). GSAS-II[19] was used to integrate the diffraction images into diffraction patterns, using a $LaB_6$ standard (NIST SRM 660c) to calibrate the sample-to-detector distance. xPDFsuite was used to calculate the PDF, and PDFgui[20] was used to simulate PDF of charged LRNMC containing molecular $O_2$ (Figure S12). XRD data for pristine/pure materials were also recorded from 0.9 mm inner diameter glass capillaries. Electrochemical data and corresponding image plots of the operando XRD data are available in Figures S6−S10.

**Rietveld Analyses.** Rietveld refinements of the pristine materials (Figures S1−S5) were carried out using the TOPAS-Academic V6 software. We used models based on the $R\bar{3}m$ space group for $Li_{1.144}Ni_{0.136}Mn_{0.544}Co_{0.136}O_2$, $Li_1Ni_{0.4}Mn_{0.4}Co_{0.2}O_2$ and $Li_1Ni_{0.80}Co_{0.15}Al_{0.05}O_2$, $P2_1/m$ for $Li_2RuO_3$,[21] and $Fm\bar{3}m$ for $Li_{1.3}Nb_{0.3}Mn_{0.4}O_2$.[5] Refined parameters included lattice parameters, isotropic atomic displacement parameters (ADP, $B_{iso}$) for TM and O sites (fixed to 1 Å$^2$ for sites solely occupied by Li), pseudo-Voigt-type peak profile parameters, and scale factor. Background was fit using an eight-term Chebyshev polynomial function. Occupancy factors were fixed based on the nominal composition, and ionic scattering factors were used based on literature-reported oxidation states. For the $R\bar{3}m$ model, we included interlayer mixing (exchange between Li and Ni between 3a and 3b sites) in the refinement. For the $P2_1/m$ model, we included exchange between Ru (4f) and Li sites (2e) in the $Li_{1/3}Ru_{2/3}$ layer to improve the fit.

For the parametric Rietveld refinements[22] of the operando XRD data recorded on LRNMC (Figure S19), details can be found in Supporting Information (Table S5).

**Small-Angle X-ray Scattering.** 7 mm diameter pressed-pellet electrodes (~20 mg) were cycled at 23.82 mA·g$^{-1}$ (~C/15), at 25 °C, in custom-made AMPIX[23]-style cells without windows. Electrodes were collected from disassembled cells after charge/discharge and placed in an airtight custom-made sample-holder for measurement. Small- and wide-angle X-ray scattering data ($\lambda$ = 0.918 Å) were recorded simultaneously at beamline 11-BM of the NSLS-II, using two area detectors placed at different sample-to-detector distances. The data were merged together to provide data in the 0.0027−3.5 Å$^{-1}$ $Q$ range. Silver behenate was used to calibrate the sample-to-detector distance. Intensities were corrected based on measured transmission.

**SAXS Modeling.** Modeling and scattering contrast calculations were carried out using the Irena package.[24] For all samples, the flat background intensity was fixed to the value of the intensity measured at $Q$ = 2.28 Å$^{-1}$. The scattering contrast of all populations was fixed to the same value ($100 \times 10^{-20}$ cm$^{-4}$). To allow for comparison between samples, the standard deviation (stdev) on the size (i.e., the width of the size distribution) was fixed to an arbitrary value as the parameter was found to be correlated to the size parameter. For all samples, the power-law decay in intensity ($I(Q) \propto Q^{-\alpha}$) at $Q$ < 0.1 Å$^{-1}$ was fit using a unified approach, as described by Beaucage.[25] This scattering is attributed to a surface fractal present in the electrode mixture. We refer to this scattering as population A. Population A was refined for all samples.

·The pristine, 4.1 V-, 4.4 V-, and 4.5 V-charged data could be adequately fit using an additional log-normal size distribution of spherical scattering domains to account for the low-intensity scattering initially present at $Q \sim 1$ Å$^{-1}$. We refer to this scattering as population B. We attribute this scattering to nanoscale features initially present in the electrode (e.g., porosity of carbon black additive and/or the initial morphology/pores of the pristine LRNMC). Population B was first refined for the pristine sample and then fixed for the 4.1 V-, 4.4 V-, and 4.5 V-charged sample except for its scale factor (Figure S13, Table S1). For all other samples described below, all parameters of population B were fixed, including the scale factor (fixed to 0.1, the value obtained for the 4.4 V-charged electrode).

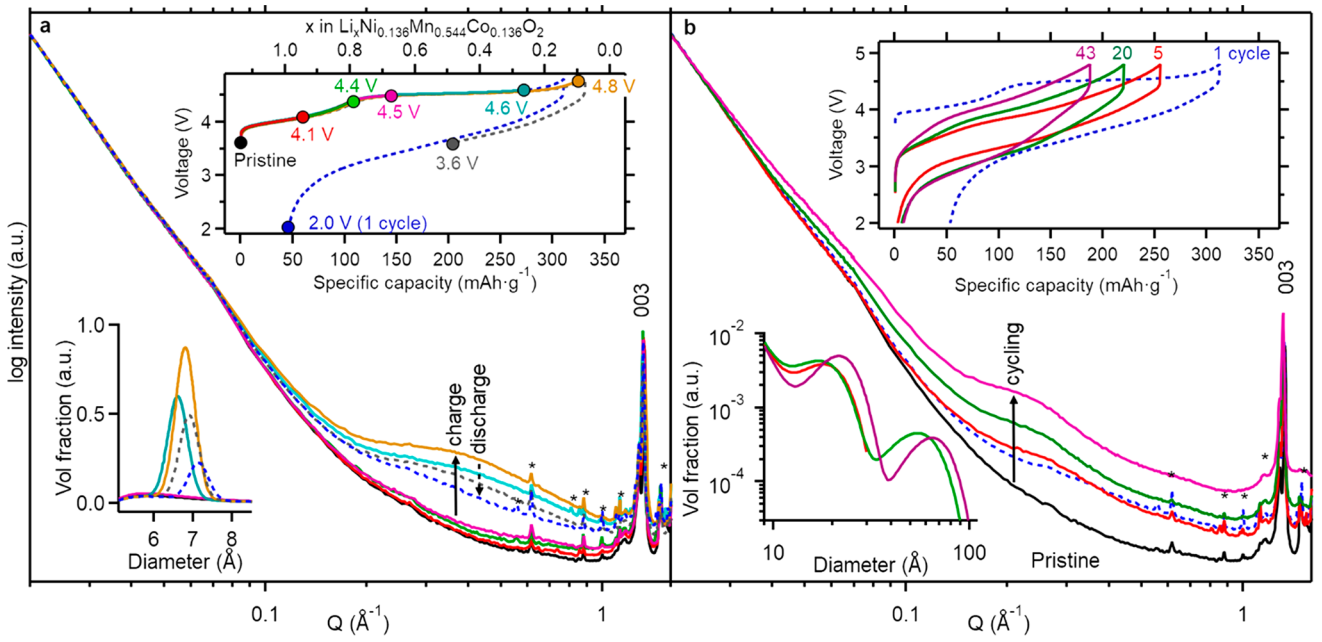


**Figure 1.** Small-angle X-ray scattering (SAXS) data recorded on $Li_{1.144}Ni_{0.136}Mn_{0.544}Co_{0.136}O_2$ at different states of charge and cycling: (a) in the first cycle and (b) after multiple cycles (4.8–2.0 V at C/15). For clarity, the data were vertically offset so that the intensity measured at $Q = 0.02$ Å$^{-1}$ was the same for all data sets. The asterisks (*) on the SAXS data denote peaks attributed to surface/electrolyte species. The corresponding charge–discharge curves and size distributions obtained from the modeling are shown in insets. Representative fits for the pristine, 4.8 V charged, 5-cycled, and 43-cycled electrodes are available in Figures S13–S16. Detailed results of the modeling are available Tables S1–S3. Because the real space dimension of the scattering object $d$ is inversely proportional to the momentum transfer $Q$ ($d = 2\pi/Q$), SAXS ($Q < 1$ Å) probes the nanoscale to microscale ($d > 6$ Å) structure of materials.

·For the electrodes charged to 4.6 and 4.8 V and discharged to 3.6 and 2.0 V, an additional population (population C) was needed to fit the broad feature that increases/decreases in intensity during charge/discharge (Figure S14, Table S2). Population C consists of a Gaussian size distribution with a spheroid form factor and a structure factor. We attribute this population to the formation of nanopores within the LRNMC crystals.

·For the cycled electrodes (5, 20, 43 cycles), only the scale factor of population C was allowed to be refined from the fit obtained after a full cycle (i.e., we speculate that the residual intensity observed after a full cycle may accumulate upon further cycling). Additional populations consisting of Gaussian size distributions with spheroid form factor were added as required to fit the additional features growing at lower $Q$ with increasing cycle number: for the 5-cycles sample, a single population (D) was enough to adequately fit the data (Figure S15), but two populations (D and E) were required to more consistently fit the 20- and 43-cycled electrodes (Figure S16, Table S3).

## RESULTS

The voltage profiles (Figure 1, insets) for $Li_{1.144}Ni_{0.136}Mn_{0.544}Co_{0.136}O_2$ (LRNMC; see Figure S1 for its characterization) are typical of LRNMC phases and match voltage profiles reported for this sample.[16] In the first cycle, two distinct charge voltage regions are evident: below 4.4 V, which is associated with TM oxidation, and above 4.4 V, which is associated with O oxidation.[1] Beyond the initial cycle, these two charge voltage regions are not distinct.

SAXS data, sensitive to nanoscale density fluctuations, show a broad feature centered at ~0.4 Å for recovered LRNMC electrodes charged above 4.5 V (Figure 1). This feature grows in intensity and shifts to lower $Q$ with increasing charge. The scattering feature reduces in intensity during the subsequent discharge but is not completely eliminated in the fully discharged sample (2.0 V), indicating that the nanoscale structural transformation is not entirely reversible under the cycling conditions used.

Part of the broad small angle scattering feature is observed in operando XRD data measured to low angle ($Q$ ~0.4 Å$^{-1}$), at angles below the first Bragg peak, 003 (Figure 2). The progressive changes in low $Q$ intensity in these operando data serve as proxy for the changes in the small angle scattering intensity throughout cycling. During charge, the integrated scattering intensity at low $Q$ (0.4 Å$^{-1}$ < $Q$ < 0.9 Å$^{-1}$) increases only at voltages above 4.5 V, that is, during the O oxidation; it does not change below 4.5 V, that is, during TM oxidation. The intensity of this feature decreases slightly during the subsequent discharge, without clear correlation to the voltage.

The SAXS feature could be modeled using a Gaussian size distribution of spherical scattering domains with an average diameter of ~7 Å (Figure 1a, inset and Figure S14). A spherical form factor for the domains yielded an adequate fit to the data provided that the model included a structure factor. Such a structure factor is indicative of scattering domains that are not infinitely dilute and have some characteristic spacing (refined here as 9 Å mean distance between the surface of the spherical domains, or 16 Å between domain centers; Table S2). Note that the scattering contrast, reflective of the density difference between the electrode particle and spherical domains, was fixed for the SAXS models. Accordingly, the real volume fractions may vary systematically from the refined values owing to the variation in the average electron density of the electrode that accompanies (de)lithiation (by 14%) (Table S4). For example, the decrease in the LRNMC's density during charge (calculated from the Rietveld refinements) will lead to a decrease in the scattering contrast with the spherical domains, biasing the volume fraction to lower values. It should also be noted that estimation of the quantitative volume fractions also

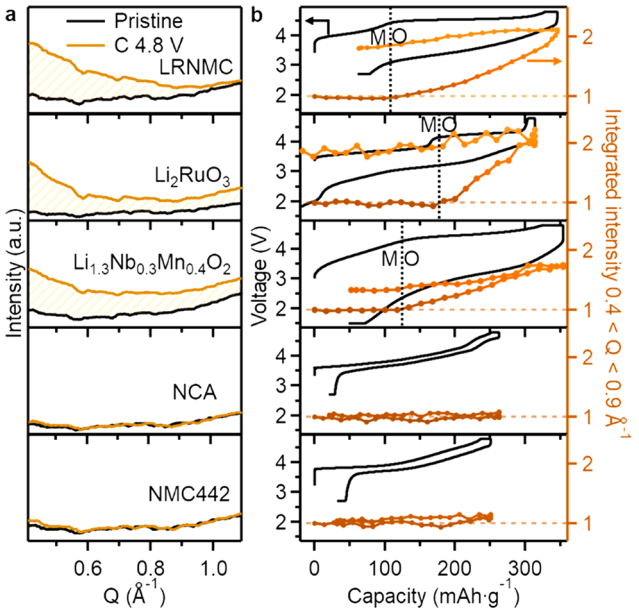


**Figure 2.** Summary of the operando synchrotron XRD data recorded during cycling of cells containing $Li_{1.144}Ni_{0.136}Mn_{0.544}Co_{0.136}O_2$ (LRNMC), $Li_2RuO_3$, $Li_{1.3}Nb_{0.3}Mn_{0.4}O_2$, $Li_1Ni_{0.80}Co_{0.15}Al_{0.05}O_2$ (NCA), and $Li_1Ni_{0.4}Mn_{0.4}Co_{0.2}O_2$ (NMC442) cathodes. (a) Comparison of the low $Q$ region of the XRD patterns collected for the pristine cells and after charging to 4.8 V. The intensity scale is the same for all. Full XRD patterns are available in Figure S11. (b) First-cycle electrochemistry and corresponding integrated XRD intensity in the 0.4–0.9 $Å^{-1}$ $Q$ range. The vertical dashed lines separate charge voltage regions M and O and are guides for the eye.

requires calibration of the SAXS intensity using a standard such as glassy carbon.[26] This intensity calibration was not performed.

The average diameter of the spherical domains increases between 4.6 and 4.8 V, as is consistent with the small shift of the SAXS feature to lower $Q$ (i.e., larger real-space dimension, $d = 2\pi/Q$). The average diameter further increases during discharge, as the total population of spheroids decreases. This observation suggests that the smallest domains are being eliminated preferentially during discharge.

SAXS data collected for discharged LRNMC electrodes following 5, 20, and 43 cycles (Figure 1b) show that the residual intensity in the SAXS feature increases with increased cycling and also shifts to lower $Q$, suggesting a larger volume of features of larger real-space dimension compared to the first cycle. The shift to lower $Q$ is reflected in an increase average spheroid diameter (14–64 Å) in models fit to the data.

Comparison of operando XRD data collected for other positive electrode materials shows that the formation of this small angle scattering feature is common to Li-rich electrode materials that exhibit O redox activity and occurs in concert with the O oxidation (Figure 2). Measurements on Li-rich layered oxide $Li_2RuO_3$ and Li-rich cation-disordered rock salt $Li_{1.3}Nb_{0.3}Mn_{0.4}O_2$ show an increase in the low-$Q$ intensity for charge to 4.8 V. The onset of this increase in scattering coincides with a cell voltage corresponding to the reported onset of O oxidation in LRNMC,[11] $Li_2RuO_3$,[27] and $Li_{1.3}Nb_{0.3}Mn_{0.4}O_2$.[28] We denote the two charge regions delimited by this change in charge compensation mechanism as "M" and "O". During subsequent discharge of the Li-rich electrodes the trends are partially reversed, with the low-$Q$ scattering intensity decreasing as discharge proceeds; however the initial intensities are not recovered. By contrast, conventional layered oxides $Li_1Ni_{0.80}Co_{0.15}Al_{0.05}O_2$ (NCA) and $Li_1Ni_{0.4}Mn_{0.4}Co_{0.2}O_2$ (NMC442) show no significant change in the low-$Q$ intensity throughout cycling.

## DISCUSSION

The growth of a small angle scattering feature, indicative of nanostructure formation, is clearly linked to O oxidation in Li-rich electrodes. It is only observed in Li-rich systems known to exhibit O redox activity. It only grows during the parts of the charge that have been shown to be associated with O oxidation. It is not observed in conventional layered oxides, despite RIXS measurements showing evidence of O redox activity in the conventional systems as well.[3]

We propose that the small angle scattering feature is linked to nanoscale density fluctuations that form within the Li-rich electrodes during O oxidation. Other potential origins of a low angle scattering feature or other nanostructure transformations can be excluded as they are inconsistent with our observations:

·A Bragg peak associated with a superstructure and crystallographic ordering of defects or vacancies can be excluded as the origin of the scattering feature. Lattice dimensions determined based on the operando synchrotron XRD data show that both the $a$ and $c$ lattice parameters (and therefore the $d$-spacing of all Bragg peaks) decrease upon charging from 4.6 to 4.8 V.[29] If the first-cycle SAXS feature was due to an ordering commensurate with the crystallographic lattice, its $d$-spacing should decrease in parallel with the lattice dimensions. Instead, the "$d$-spacing" of the broad SAXS feature increases upon charging from 4.6 V ($d$ = 17.5 Å) to 4.8 V ($d$ = 18.7 Å). This directly contradicts the behavior expected for superstructure formation.

·Microstructural changes induced by cracking[30,31] or surface reconstruction[32,33] can be excluded as the principal origin of the SAXS signal in the Li-rich systems based on the absence of this signal for NCA and NMC systems, for which such microstructural changes have been demonstrated. Notably, the extent of surface reconstruction (Li–TM antisite defects localized in a thin surface layer) is comparable for conventional[32,33] and Li-rich layered oxides,[34] with the surface layer being typically 2–3 nm thick. Such thin surface layers represent too small a fraction of the particle to contribute significantly to the bulk scattering intensity.

·Similarly, cathode–electrolyte interface (CEI) formation can be excluded as the principal origin of the SAXS signal, as surface-sensitive X-ray photoelectron spectroscopy measurements on LRNMC do not show any sudden increase in the amount of surface species in the voltage regime associated with O oxidation.[35]

Hence, the nanoscale density fluctuations are associated with lower density nanoscale domains that form throughout the electrode particles, with commensurate densification of the surrounding material. While densified regions can form within LRNMC as a consequence of TM migration during O oxidation,[13] this cannot be the sole origin of the SAXS feature. Such a scenario, in which the SAXS signal is due to contrast between densified spinel-like regions[36] and delithiated LRNMC, is inconsistent with our results. The density of discharged LRNMC (4.26 $g/cm^3$) is close to that of hypothetical densified domains of spinel-like $Li_{0.23}Mn_2O_4$ (4.45 $g/cm^3$) such that the scattering contrast between these domains would approach zero upon discharge, effectively

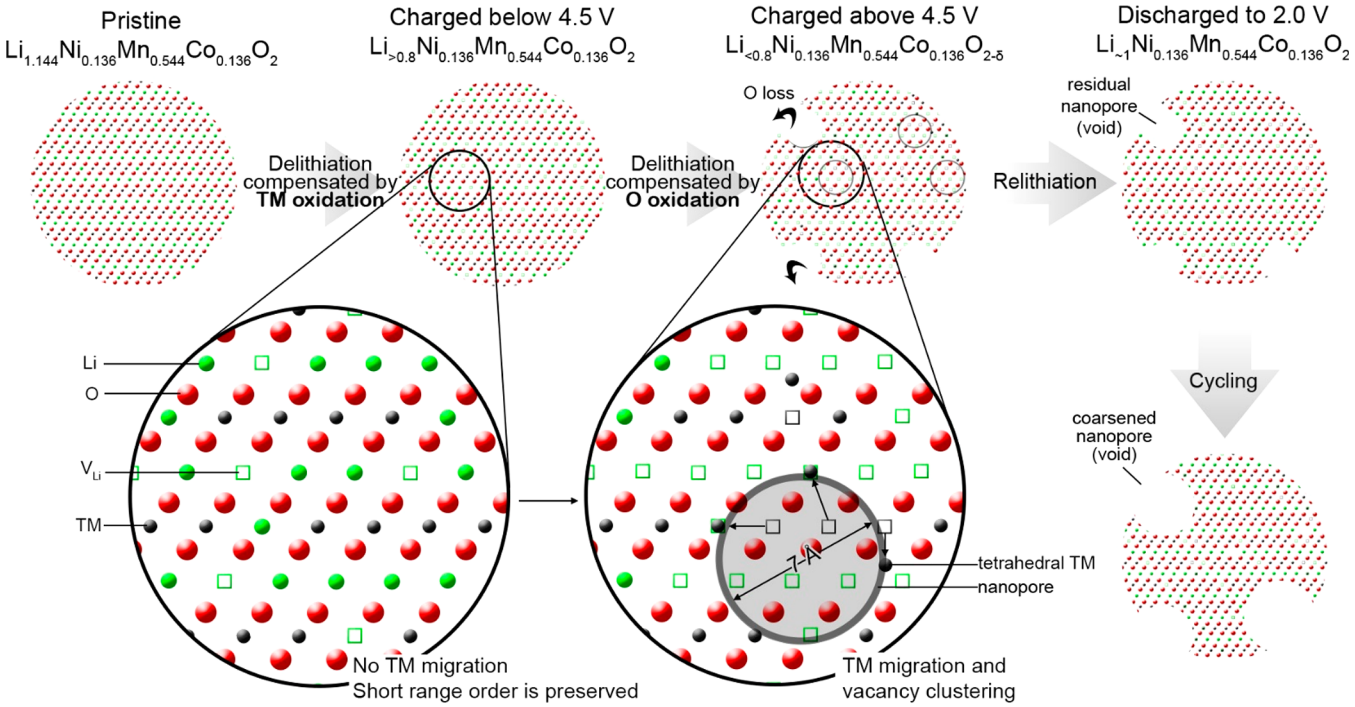


**Figure 3.** Schematic illustration of the proposed mechanism. Conventional charge/delithiation below 4.5 V is compensated by transition metal oxidation, leaving lithium vacancies $V_{Li}$. Charge/delithiation in the 4.5 V plateau is accompanied by the migration of TMs to vacant octahedral and tetrahedral sites of the Li layer (interlayer migration) and vacant octahedral sites of the TM layer (intralayer migration). This results in the formation of ~7 Å nanopores at ~9 Å spacing. Irreversible oxygen loss converts reversible nanopores to unreactive nanovoids; after discharge, nanopores are eliminated as TMs migrate back to TM layers. Upon further cycling, unreactive nanovoids coarsen to form larger nanovoids as O loss persists.

suppressing the SAXS signal (Table S4). Therefore, we attribute the SAXS signal to contrast between lower density nanoscale domains and the LRNMC. For simplicity, we refer to the lower density nanoscale domains as "nanopores", although we do not exclude the possibility that these nanoscale domains first contain oxidized O species and can evolve into nanovoids upon cycling. This is discussed in more detail later.

Forming these ~7 Å diameter nanopores required TM migration on the length scale of a few Å. A detailed analysis of the operando XRD using the Rietveld method shows significant TM migration to Li layers (i.e., interlayer migration) during O oxidation. The refinements suggest that ~18% of TMs (~0.15/0.816) migrate from their original octahedral ($O_h$) sites in the TM layer to both $O_h$ and tetrahedral ($T_d$) sites of the Li layer after charge to 4.8 V (Figure S19). Such substantial TM migration has been observed in other studies and is evident as the loss of the TM honeycomb-like superstructure ordering present in the pristine LRNMC structure (Figure S18).[11,12] The superstructure ordering of TMs in the TM layers is characterized by the presence of Bragg peaks in the 1.4–2.1 $Å^{-1}$ $Q$ range of the operando XRD data. These superstructure peaks are eliminated during charge above 4.5 V (Figure S18d).[11] While the majority of $T_d$ TMs migrate back to original $O_h$ sites during discharge, TM migration to $O_h$ sites of the Li layer seems mostly irreversible.

Such TM migration has also been reported for $Li_2RuO_3$.[37] Nanopore formation in cation-disordered rocksalt $Li_{1.3}Nb_{0.3}Mn_{0.4}O_2$ suggests that a three-dimensional diffusion of TMs needs to be considered in Li-rich materials. In the Li-rich cation-disordered rocksalt structure, TM and Li ions occupy the TM and Li layers indiscriminately so that the TM diffusion that likely occurs during O oxidation cannot be resolved using XRD as has been done for the layered structures of LRNMC and $Li_2RuO_3$. Nanopore formation in the cation-disordered rocksalt structure of Li-rich $Li_{1.3}Nb_{0.3}Mn_{0.4}O_2$ and absence of nanopore formation in the layered structure of stoichiometric NMC/NCA suggest that TMs are able to migrate not only between layers but also within layers of Li-rich materials with a layered structure (intralayer migration). This three-dimensional diffusion of TMs in the Li-rich structures may be allowed by the presence of an increasing amount of octahedral vacancies during delithiation and may be triggered by the O oxidation reaction. This proposed mechanism of interlayer and intralayer migration of TMs resulting in nanopore formation is illustrated in Figure 3 for LRNMC. Despite reports of O oxidation in stoichiometric NMC,[3] nanopore formation is not observed as TM migration is prevented in the absence of a significant amount of vacant octahedral sites in TM layers.

The 4.5 V plateau is reminiscent of the electrochemical profile of a pseudo two-phase reaction; we propose that this is associated with the transformation from a uniform to nanostructured morphology, as described above. The absence of this plateau during discharge and subsequent cycles is consistent with the irreversible loss of the initial cation order, in agreement with the structural analyses.

The characteristics of the nanopores (being voids or containing oxygen) are an open question that can be addressed, in part, by considering the degree to which the oxygen lost from the system (i.e., associated with an irreversible loss in capacity) is also "missing" from the crystalline LRNMC lattice. If the O loss in these cases match, the nanopores must be void; if not, the nanopores likely contained trapped O species.

The capacity generated by reversible lattice O oxidation (i.e., excluding irreversible O loss) was previously estimated to account for 76% [0.54/0.71 electrons ($e^-$) per formula unit] of the total capacity generated by the 4.5 V plateau from mass spectrometry,[8] or 73% (0.38/0.52 $e^-$) from RIXS measurements.[6] Similar trends have been reported for Co-free samples.[9] In each of these prior studies, irreversible O loss was estimated to correspond to 0.17−0.14 $e^-$, extracted throughout the 4.5 V plateau. This matches the first cycle capacity loss (~0.14 $e^-$, ~50 mAh/g) observed here, suggesting that reversible lattice O oxidation equates to ~0.5 $e^-$ in our case. This loss in capacity is not observed when the LRNMC electrode is charged in the TM-redox regime below 4.5 V.[11,38] Note that the irreversible O loss mostly occurs beyond the sloping O oxidation plateau, above 4.6 V, as overpotential rapidly increases to 4.8 V.[8]

Within the crystalline LRNMC lattice, Rietveld analysis of the operando XRD data further suggests that the O site occupancy decreases during charge (Figure S19).[29] The reduced O occupancy after charge to 4.8 V corresponds to vacancies at ~24% of O sites. Since irreversible O loss involves a two-electron process (e.g., $O^{2-} \rightarrow {}^1/_2O_2 + 2e^-$), the 0.14 $e^-$ estimated to be due to O loss should correspond to a 3.5% decrease in O occupancy. This is much less than the ~24% decrease in the O occupancy indicated by the XRD analysis. Therefore, irreversible O loss from the lattice is not the primary cause for the decrease in O occupancy during O oxidation. Instead, the reduced O site occupancy is primarily due to the displacement of O atoms beyond the ellipsoid defined by the atomic displacement parameters. Our attempts to refine a disordered structural model in which the O was displaced from the original site (i.e., displaced along $z$ similar to the off-centered TM sites) from the operando XRD data were unsuccessful. This suggests either that the displacement of O atoms is an noncooperative local phenomenon that cannot be captured by XRD, as previously postulated based on neutron PDF measurements,[39] or that the oxidized O atoms may no longer be commensurate with the lattice and are trapped within the nanopores.

Recently, O oxidation was proposed to lead to formation of trapped molecular $O_2$.[40] To explore the sensitivity of our data to the potential presence of $O_2$, we calculated a differential pair distribution function (dPDF) corresponding to the change in the atom−atom distances in LRNMC during the 4.5 V plateau (Figure S12). Simulations of a dPDF, in which 12% molecular $O_2$ forms, suggest that we should be able to observe a peak due to molecular $O_2$ if it were to form. However, our data do not show evidence of a peak at ~1.2 Å, that is the O−O distance in molecular $O_2$, and thus, our data do not support the hypothesis that molecular $O_2$ is contained within the nanopores. Further analyses are needed to identify the nature of the oxidized species within the nanopores following the first cycle.

The elimination of the SAXS feature following discharge, and the reversibility of nanostructuring, is less complete in the sample studied operando, where a 2 h hold at 4.8 V was applied to the cell. We hypothesize that the different degrees to which these are eliminated in the *ex situ* relative to the operando measurements may be due to a greater O loss, that is, a conversion of O-containing nanopores to voids (Figure S17). It is likely that additional O loss from the LRNMC occurred during the 4.8 V hold. As nanopore elimination involves reduction of the oxidized O species during discharge, any additional O loss upon charge should result in an increased amount of residual nanopores. It is conceivable that during the potentiostatic hold oxidized O species within near-surface nanopores can diffuse to the surface and are released in the electrolyte as gaseous $O_2$, effectively converting reversible O-containing nanopores to irreversible nanovoids.

This mechanism may explain recent electron microscopy studies that reveal the presence of >100 Å nanovoids within the LRNMC particles after extended cycling.[36,41] The large nanovoids appear to first form near the surface and progressively spread to the interior of the LRNMC grains. We confirm the presence of larger low-density nanoscale domains within the bulk of LRNMC upon repeated cycling. For the 20 and 43 times cycled samples, additional spherical populations of >50 Å diameter are needed to consistently fit the data. Unlike for the first-cycle ~7 Å nanopores, fitting those larger distributions does not require the use of a structure factor, showing that these features are more dilute or irregularly spaced (Table S3). This result is consistent with the reported electron microscopy studies and suggests that the residual ~7 Å nanovoids following the initial cycle may serve as nuclei for the growth of larger domains in subsequent cycles, as O loss persists. Over multiple cycles, this leads to a coarsening of the nanovoid domains in a mechanism reminiscent of Ostwald ripening (Figure 3).

## CONCLUSIONS

Our results suggest that nanopore formation is a structural consequence of O oxidation in Li-rich 3*d* and 4*d* transition metal oxide cathodes. The formation of nanopores is likely facilitated by the cation mobility and disorder within the cathode. The specific mechanism for cation migration and vacancy clustering leading to the formation of nanopores, as well as the precise composition of the nanopores, remains to be defined.

Our results link the structural consequences of O oxidation in an individual cycle to large-scale structure changes that were previously only detected after prolonged cycling; these large-scale structure changes have been implicated in performance degradation. In an individual cycle, nanopore formation appears to be a reversible process, with any loss of O from the electrode likely preventing nanopore elimination during discharge. Residual nanovoids in the cathode may accumulate and coarsen upon cycling.

## AUTHOR INFORMATION


### Corresponding Author

**Karena W. Chapman** − *Department of Chemistry, Stony Brook University, Stony Brook, New York 11794, United States;* orcid.org/0000-0002-8725-5633; Email: karena.chapman@stonybrook.edu

## Authors

**Antonin Grenier** − *Department of Chemistry, Stony Brook University, Stony Brook, New York 11794, United States;* orcid.org/0000-0001-8404-3240

**Gabrielle E. Kamm** − *Department of Chemistry, Stony Brook University, Stony Brook, New York 11794, United States*

**Yixuan Li** − *Department of Nano Engineering, University of California San Diego (UCSD), La Jolla, California 92093, United States*

**Hyeseung Chung** − *Department of Nano Engineering, University of California San Diego (UCSD), La Jolla, California 92093, United States*

**Ying Shirley Meng** − *Department of Nano Engineering, University of California San Diego (UCSD), La Jolla, California 92093, United States;* orcid.org/0000-0001-8936-8845


## ■ ACKNOWLEDGMENTS


This work was supported as part of the NorthEast Center for Chemical Energy Storage (NECCES), an Energy Frontier Research Center funded by the U.S. Department of Energy (DOE), Office of Science, Basic Energy Sciences (BES) under Award DESC0012583. This research used resources at the 28-ID-1 and 11-BM beamlines of the National Synchrotron Light Source II, a U.S. Department of Energy (DOE) Office of Science User Facility operated for the DOE Office of Science by Brookhaven National Laboratory under Contract DE-SC0012704. The NMC442 powder was provided by the Cell Analysis, Modeling, and Prototyping (CAMP) Facility at Argonne, which is supported by the U.S. Department of Energy (DOE), Office of Energy Efficiency and Renewable Energy, Vehicle Technologies Office. We acknowledge Hui Zhong for support with the XRD measurements, and Ruipeng Li and Masafumi Fukuto for support with the SAXS measurements.


## ■ REFERENCES


(1) Assat, G.; Tarascon, J. M. Fundamental Understanding and Practical Challenges of Anionic Redox Activity in Li-Ion Batteries. *Nat. Energy* **2018**, *3* (5), 373−386.

(2) Radin, M. D.; Vinckeviciute, J.; Seshadri, R.; Van der Ven, A. Manganese Oxidation as the Origin of the Anomalous Capacity of Mn-Containing Li-Excess Cathode Materials. *Nat. Energy* **2019**, *4* (8), 639−646.

(3) Lee, G.; Wu, J.; Kim, D.; Cho, K.; Cho, M.; Yang, W.; Kang, Y. Reversible Anionic Redox Activities in Conventional $LiNi_{1/3}Co_{1/3}Mn_{1/3}O_2$ Cathodes. *Angew. Chem., Int. Ed.* **2020**, *59* (22), 8681−8688.

(4) Hu, E.; Li, Q.; Wang, X.; Meng, F.; Liu, J.; Zhang, J.; Page, K.; Xu, W.; Gu, L.; Xiao, R.; Li, H.; Huang, X.; Chen, L.; Yang, W.; Yu, X.; Yang, X.-Q. Oxygen-Redox Reactions in $LiCoO_2$ Cathode without O−O Bonding during Charge-Discharge. *Joule* **2021**, *5*, 720−736.

(5) Yabuuchi, N.; Takeuchi, M.; Nakayama, M.; Shiiba, H.; Ogawa, M.; Nakayama, K.; Ohta, T.; Endo, D.; Ozaki, T.; Inamasu, T.; Sato, K.; Komaba, S. High-Capacity Electrode Materials for Rechargeable Lithium Batteries: $Li_3NbO_4$-Based System with Cation-Disordered Rocksalt Structure. *Proc. Natl. Acad. Sci. U. S. A.* **2015**, *112* (25), 7650−7655.

(6) Dai, K.; Wu, J.; Zhuo, Z.; Li, Q.; Sallis, S.; Mao, J.; Ai, G.; Sun, C.; Li, Z.; Gent, W. E.; Chueh, W. C.; Chuang, Y.-d.; Zeng, R.; Shen, Z.-x.; Pan, F.; Yan, S.; Piper, L. F. J.; Hussain, Z.; Liu, G.; Yang, W. High Reversibility of Lattice Oxygen Redox Quantified by Direct Bulk Probes of Both Anionic and Cationic Redox Reactions. *Joule* **2019**, *3* (2), 518−541.

(7) Qiu, B.; Zhang, M.; Lee, S.-Y.; Liu, H.; Wynn, T. A.; Wu, L.; Zhu, Y.; Wen, W.; Brown, C. M.; Zhou, D.; Liu, Z.; Meng, Y. S. Metastability and Reversibility of Anionic Redox-Based Cathode for High-Energy Rechargeable Batteries. *Cell Reports Phys. Sci.* **2020**, *1* (3), 100028.

(8) Luo, K.; Roberts, M. R.; Hao, R.; Guerrini, N.; Pickup, D. M.; Liu, Y. S.; Edström, K.; Guo, J.; Chadwick, A. V.; Duda, L. C.; Bruce, P. G. Charge-Compensation in 3*d*-Transition-Metal-Oxide Intercalation Cathodes through the Generation of Localized Electron Holes on Oxygen. *Nat. Chem.* **2016**, *8* (7), 684−691.

(9) Luo, K.; Roberts, M. R.; Guerrini, N.; Tapia-Ruiz, N.; Hao, R.; Massel, F.; Pickup, D. M.; Ramos, S.; Liu, Y.-S.; Guo, J.; Chadwick, A. V.; Duda, L. C.; Bruce, P. G. Anion Redox Chemistry in the Cobalt Free 3d Transition Metal Oxide Intercalation Electrode $Li[Li_{0.2}Ni_{0.2}Mn_{0.6}]O_2$. *J. Am. Chem. Soc.* **2016**, *138* (35), 11211−11218.

(10) Sathiya, M.; Rousse, G.; Ramesha, K.; Laisa, C. P.; Vezin, H.; Sougrati, M. T.; Doublet, M. L.; Foix, D.; Gonbeau, D.; Walker, W.; Prakash, A. S.; Ben Hassine, M.; Dupont, L.; Tarascon, J. M. Reversible Anionic Redox Chemistry in High-Capacity Layered-Oxide Electrodes. *Nat. Mater.* **2013**, *12* (9), 827−835.

(11) Gent, W. E.; Lim, K.; Liang, Y.; Li, Q.; Barnes, T.; Ahn, S. J.; Stone, K. H.; McIntire, M.; Hong, J.; Song, J. H.; Li, Y.; Mehta, A.; Ermon, S.; Tyliszczak, T.; Kilcoyne, D.; Vine, D.; Park, J. H.; Doo, S. K.; Toney, M. F.; Yang, W.; Prendergast, D.; Chueh, W. C. Coupling between Oxygen Redox and Cation Migration Explains Unusual Electrochemistry in Lithium-Rich Layered Oxides. *Nat. Commun.* **2017**, *8* (1), 2091.

(12) Kleiner, K.; Strehle, B.; Baker, A. R.; Day, S. J.; Tang, C. C.; Buchberger, I.; Chesneau, F. F.; Gasteiger, H. A.; Piana, M. Origin of High Capacity and Poor Cycling Stability of Li-Rich Layered Oxides: A Long-Duration in Situ Synchrotron Powder Diffraction Study. *Chem. Mater.* **2018**, *30* (11), 3656−3667.

(13) Yin, W.; Grimaud, A.; Rousse, G.; Abakumov, A. M.; Senyshyn, A.; Zhang, L.; Trabesinger, S.; Iadecola, A.; Foix, D.; Giaume, D.; Tarascon, J.-M. Structural Evolution at the Oxidative and Reductive Limits in the First Electrochemical Cycle of $Li_{1.2}Ni_{0.13}Mn_{0.54}Co_{0.13}O_2$. *Nat. Commun.* **2020**, *11* (1), 1252.

(14) Wang, L.; Dai, A.; Xu, W.; Lee, S.; Cha, W.; Harder, R.; Liu, T.; Ren, Y.; Yin, G.; Zuo, P.; Wang, J.; Lu, J.; Wang, J. Structural Distortion Induced by Manganese Activation in a Lithium-Rich Layered Cathode. *J. Am. Chem. Soc.* **2020**, *142* (35), 14966−14973.

(15) Singer, A.; Zhang, M.; Hy, S.; Cela, D.; Fang, C.; Wynn, T. A.; Qiu, B.; Xia, Y.; Liu, Z.; Ulvestad, A.; Hua, N.; Wingert, J.; Liu, H.; Sprung, M.; Zozulya, A. V.; Maxey, E.; Harder, R.; Meng, Y. S.; Shpyrko, O. G. Nucleation of Dislocations and Their Dynamics in Layered Oxide Cathode Materials during Battery Charging. *Nat. Energy* **2018**, *3*, 641−647.

(16) Lebens-Higgins, Z. W.; Vinckeviciute, J.; Wu, J.; Faenza, N. V.; Li, Y.; Sallis, S.; Pereira, N.; Meng, Y. S.; Amatucci, G. G.; Van Der Ven, A.; Yang, W.; Piper, L. F. J. Distinction between Intrinsic and X-Ray-Induced Oxidized Oxygen States in Li-Rich 3d Layered Oxides and $LiAlO_2$. *J. Phys. Chem. C* **2019**, *123* (21), 13201−13207.

(17) Faenza, N. V.; Bruce, L.; Lebens-Higgins, Z. W.; Plitz, I.; Pereira, N.; Piper, L. F. J.; Amatucci, G. G. Editors' Choice—Growth of Ambient Induced Surface Impurity Species on Layered Positive Electrode Materials and Impact on Electrochemical Performance. *J. Electrochem. Soc.* **2017**, *164* (14), A3727−A3741.

(18) Liu, H.; Allan, P. K.; Borkiewicz, O. J.; Kurtz, C.; Grey, C. P.; Chapman, K. W.; Chupas, P. J. A Radially Accessible Tubular in Situ X-Ray Cell for Spatially Resolved Operando Scattering and Spectroscopic Studies of Electrochemical Energy Storage Devices. *J. Appl. Crystallogr.* **2016**, *49* (5), 1665−1673.

(19) Toby, B. H.; Von Dreele, R. B. GSAS-II: The Genesis of a Modern Open-Source All Purpose Crystallography Software Package. *J. Appl. Crystallogr.* **2013**, *46* (2), 544−549.
(20) Farrow, C. L.; Juhas, P.; Liu, J. W.; Bryndin, D.; Božin, E. S.; Bloch, J.; Proffen, T.; Billinge, S. J. L. PDFfit2 and PDFgui: Computer Programs for Studying Nanostructure in Crystals. *J. Phys.: Condens. Matter* **2007**, *19* (33), 335219.
(21) Reeves, P. J.; Seymour, I. D.; Griffith, K. J.; Grey, C. P. Characterizing the Structure and Phase Transition of $Li_2RuO_3$ Using Variable-Temperature $^{17}O$ and $^{7}Li$ NMR Spectroscopy. *Chem. Mater.* **2019**, *31* (8), 2814−2821.
(22) Stinton, G. W.; Evans, J. S. O. Parametric Rietveld Refinement. *J. Appl. Crystallogr.* **2007**, *40* (1), 87−95.
(23) Borkiewicz, O. J.; Shyam, B.; Wiaderek, K. M.; Kurtz, C.; Chupas, P. J.; Chapman, K. W. The AMPIX Electrochemical Cell: A Versatile Apparatus for in Situ X-Ray Scattering and Spectroscopic Measurements. *J. Appl. Crystallogr.* **2012**, *45* (6), 1261−1269.
(24) Ilavsky, J.; Jemian, P. R. Irena: Tool Suite for Modeling and Analysis of Small-Angle Scattering. *J. Appl. Crystallogr.* **2009**, *42* (2), 347−353.
(25) Beaucage, G. Approximations Leading to a Unified Exponential/Power-Law Approach to Small-Angle Scattering. *J. Appl. Crystallogr.* **1995**, *28* (6), 717−728.
(26) Zhang, F.; Ilavsky, J.; Long, G. G.; Quintana, J. P. G.; Allen, A. J.; Jemian, P. R. Glassy Carbon as an Absolute Intensity Calibration Standard for Small-Angle Scattering. *Metall. Mater. Trans. A* **2010**, *41* (5), 1151−1158.
(27) Li, B.; Shao, R.; Yan, H.; An, L.; Zhang, B.; Wei, H.; Ma, J.; Xia, D.; Han, X. Understanding the Stability for Li-Rich Layered Oxide $Li_2RuO_3$ Cathode. *Adv. Funct. Mater.* **2016**, *26* (9), 1330−1337.
(28) Kan, W. H.; Chen, D.; Papp, J. K.; Shukla, A. K.; Huq, A.; Brown, C. M.; McCloskey, B. D.; Chen, G. Unravelling Solid-State Redox Chemistry in $Li_{1.3}Nb_{0.3}Mn_{0.4}O_2$ Single-Crystal Cathode Material. *Chem. Mater.* **2018**, *30* (5), 1655−1666.
(29) Zuba, M. J.; Grenier, A.; Lebens-Higgins, Z.; Fajardo, G. J. P.; Li, Y.; Ha, Y.; Zhou, H.; Whittingham, M. S.; Yang, W.; Meng, Y. S.; Chapman, K. W.; Piper, L. F. J. Whither Mn Oxidation in Mn-Rich Alkali-Excess Cathodes? *ACS Energy Lett.* **2021**, *6*, 1055−1064.
(30) Yan, P.; Zheng, J.; Gu, M.; Xiao, J.; Zhang, J. G.; Wang, C. M. Intragranular Cracking as a Critical Barrier for High-Voltage Usage of Layer-Structured Cathode for Lithium-Ion Batteries. *Nat. Commun.* **2017**, *8*, 14101.
(31) Liu, H.; Wolf, M.; Karki, K.; Yu, Y.; Stach, E. A.; Cabana, J.; Chapman, K. W.; Chupas, P. J. Intergranular Cracking as a Major Cause of Long-Term Capacity Fading of Layered Cathodes. *Nano Lett.* **2017**, *17* (6), 3452−3457.
(32) Faenza, N. V.; Lebens-Higgins, Z. W.; Mukherjee, P.; Sallis, S.; Pereira, N.; Badway, F.; Halajko, A.; Ceder, G.; Cosandey, F.; Piper, L. F. J.; Amatucci, G. G. Electrolyte-Induced Surface Transformation and Transition-Metal Dissolution of Fully Delithiated $LiNi_{0.8}Co_{0.15}Al_{0.05}O_2$. *Langmuir* **2017**, *33*, 9333−9353.
(33) Lin, F.; Markus, I. M.; Nordlund, D.; Weng, T.-C.; Asta, M. D.; Xin, H. L.; Doeff, M. M. Surface Reconstruction and Chemical Evolution of Stoichiometric Layered Cathode Materials for Lithium-Ion Batteries. *Nat. Commun.* **2014**, *5*, 3529.
(34) Boulineau, A.; Simonin, L.; Colin, J.-F.; Bourbon, C.; Patoux, S. First Evidence of Manganese−Nickel Segregation and Densification upon Cycling in Li-Rich Layered Oxides for Lithium Batteries. *Nano Lett.* **2013**, *13* (8), 3857−3863.
(35) Hekmatfar, M.; Kazzazi, A.; Eshetu, G. G.; Hasa, I.; Passerini, S. Understanding the Electrode/Electrolyte Interface Layer on the Li-Rich Nickel Manganese Cobalt Layered Oxide Cathode by XPS. *ACS Appl. Mater. Interfaces* **2019**, *11* (46), 43166−43179.
(36) Yan, P.; Zheng, J.; Tang, Z. K.; Devaraj, A.; Chen, G.; Amine, K.; Zhang, J. G.; Liu, L. M.; Wang, C. Injection of Oxygen Vacancies in the Bulk Lattice of Layered Cathodes. *Nat. Nanotechnol.* **2019**, *14* (6), 602−608.
(37) Zheng, F.; Zheng, S.; Zhang, P.; Zhang, X.; Wu, S.; Yang, Y.; Zhu, Z. Z. Impact of Structural Transformation on Electrochemical Performances of Li-Rich Cathode Materials: The Case of $Li_2RuO_3$. *J. Phys. Chem. C* **2019**, *123* (22), 13491−13499.
(38) Tran, N.; Croguennec, L.; Ménétrier, M.; Weill, F.; Biensan, P.; Jordy, C.; Delmas, C. Mechanisms Associated with the "Plateau" Observed at High Voltage for the Overlithiated $Li_{1.12}(Ni_{0.425}Mn_{0.425}Co_{0.15})_{0.88}O_2$ System. *Chem. Mater.* **2008**, *20* (15), 4815−4825.
(39) Zhao, E.; Zhang, M.; Wang, X.; Hu, E.; Liu, J.; Yu, X.; Olguin, M.; Wynn, T. A.; Meng, Y. S.; Page, K.; Wang, F.; Li, H.; Yang, X. Q.; Huang, X.; Chen, L. Local Structure Adaptability through Multi Cations for Oxygen Redox Accommodation in Li-Rich Layered Oxides. *Energy Storage Mater.* **2020**, *24*, 384−393.
(40) House, R. A.; Rees, G. J.; Pérez-Osorio, M. A.; Marie, J.; Boivin, E.; Robertson, A. W.; Nag, A.; Garcia-Fernandez, M.; Zhou, K.; Bruce, P. G. First-Cycle Voltage Hysteresis in Li-Rich 3*d* Cathodes Associated with Molecular $O_2$ Trapped in the Bulk. *Nat. Energy* **2020**, *5* (10), 777−785.
(41) Hu, E.; Yu, X.; Lin, R.; Bi, X.; Lu, J.; Bak, S.; Nam, K. W.; Xin, H. L.; Jaye, C.; Fischer, D. A.; Amine, K.; Yang, X. Q. Evolution of Redox Couples in Li- and Mn-Rich Cathode Materials and Mitigation of Voltage Fade by Reducing Oxygen Release. *Nat. Energy* **2018**, *3* (8), 690−698.